Remarkable Acceleration of Biomolecules Enrichment and Detection with Motorized Opto-plasmonic Microsensors and the Working Mechanism

Jianhe Guo[1#], Zexi Liang[1#], Kwanoh Kim[2], Peter Vandeventer[3], and Donglei (Emma) Fan[1,2*]

[1] Texas Materials Institute and Materials Science and Engineering Program, The University of Texas at Austin, Austin, TX 78712, USA

[2] Department of Mechanical Engineering, The University of Texas at Austin, Austin, TX 78712, USA

[3]Defense Threat Reduction Agency, Fort Belvoir, VA 22060, USA

Abstract

Vigorous research efforts have advanced the state-of-the-art nanosensors with ultrahigh sensitivity for bioanalysis. However, a dilemmatic challenge remains. It is extremely difficult to obtain dually sensitive and high-speed nanosensors for the detection of low-concentration molecules in aqueous samples. Herein, we report how the controlled mechanical rotation (or rotary motorization) of designed opto-plasmonic microsensors can substantially and robustly accelerate the enrichement and detection speed of deoxyribonucleic acid (DNA) with retained high sensitivity. At least 4-fold augment of capture speed of DNA molecules is obtained from a microsensor rotating at 1200 rpm. Theoretical analysis and modeling shed light on the underlying working mechanism, governed by the molecule-motor-flow interaction, as well as its application range and limitation. This work provides a new device scheme that alleviates the dilemmatic challenge in biomolecule sensing, and also the understanding of the complex interactions of molecule and moving microobject in suspension. The results can assist the rational design of efficient microrobotic systems for the capture, translocation, sensing, and release of biocargos.

Introduction

Although substantial efforts have advanced nanosensors with single-molecule sensitivity,(*1-5*) the high sensitivity owing to the small sensing area of a nanosensor comes at the expense of adversely long detection time for low-concentration analyte molecules. A decade of research shows that regardless of the employed sensing mechanism (optical, mechanical, or electrical), the best nanosensors that have been made can take *hours* to detect molecules of 1 pM– 1 fM.(*6-10*) This pressing issue has substantially hindered the potential of nanosensors for practical applications. Theoretical calculations show that when analyte solutions are dilute, a depletion layer is formed quickly around a nanosensor, across which analyte molecules transport to the sensor surface by a slow diffusion process driven by the concentration gradient. This in turn further increases the size of the depletion region. As a result, the speed of molecule transport and attachment to a nanosensor is not only low but also continuously reduces with time. An upper-bound estimation shows that the minimum detection time of a single molecule event in 1 fM analyte solution is at least *one hour* for a commonly used 1 μm sized sensor.(*11*) The required detection time increases rapidly when the sensor dimensions are further reduced to nanometer scales.(*12*) It is intrinsically difficult to make nanosensors that are both ultrasensitive and high-speed for detecting molecules of low concentration.

The rapid development of artificial micro/nanomachines (or micro/nanomotors) made of synthesized micro/nanoscale building blocks has unveiled rich fundamental science(*13, 14*) and a wealth of unprecedented applications,(*15-17*) owing to their unique attribute of locomotion. A variety of micro/nanomachines have been made for biomedical applications that are powered by energy sources ranging from chemical reactions to magnetic, electric, and acoustic fields.(*18-27*) Notably, the enhancement of biodetection speed has been observed from motorized micro/nanosensors (*28-31*), such as linearly translocating fluorescent microparticle and microtube sensors. Offering the convenience in actuation, however, the constantly changed position of a translocating sensor presents challenges in monitoring the dynamic signals of molecules for a long duration. While a durable detection is important for the sensing of low-concentration molecules. A linearly moving sensor also often requires a large operation footprint of a feature dimension of a hundred micrometer, which entails a relatively large sampling volume. To overcome the barrier of low-concentration biosensing, it is pivotal to explore an innovative sensing scheme that can enhance detection speed without compromising its high sensitivity and offer long time and position deterministic detection. Particularly, the fixed sensing position with a small footprint, *e.g.*, the size of a sensor itself, is imperative for minute sample analysis and compact device integration. Besides the demand for a feasible device scheme, it is essential to understand the underlying working principle, its controlling factors, and application range.

Here we report the design, fabrication, and application of a rotary micromotor-sensor system for robust augment of capture and detection speed of biomolecules, *i.e.*, salmon sperm DNA, with Surface Enhanced Raman Scattering (SERS) spectroscopy. The sensitive, durable, and position-stable rotating sensors continuously monitor the dynamic capture process of DNA molecules *in situ* and in quasi-real-time. The rotation notably accelerates the capture efficiency of the DNA molecules by at least 4 folds at 1200 rpm, and boosts the detection speed of low-concentration DNAs (80 nM) by 3 times at 630 rpm. Theoretical analysis and modeling unveil the working mechanism, governed by the complex molecule-motor-flow interaction, and suggest its application range.

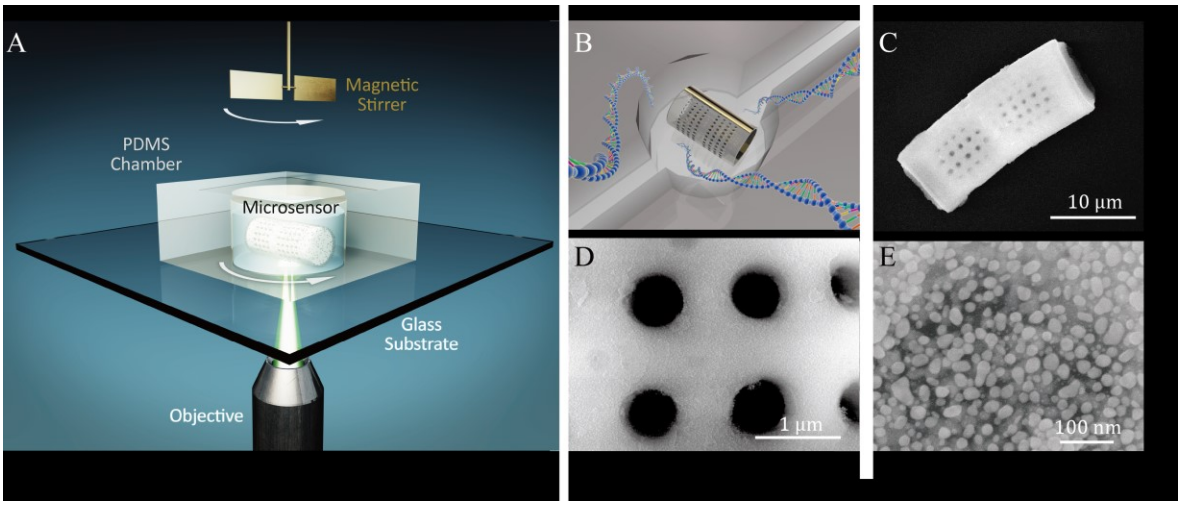

Figure. 1. Design and fabrication of Micromotor-sensors. (**A-B**) Schematic of a rotating biosilica opto-plasmonic microsensor in a well with DNA molecules. (**C-D**) Scanning electron microscopy (SEM) images of the diatom frustules with periodic nanopores, and (**E**) the dense surface-distributed Ag nanoparticles.

Results

A bioenabled opto-plasmonic enhanced micromotor-sensor is designed consisting of a diatom frustule as the sensor body, uniformly distributed plasmonic Ag nanoparticles on the surface for SERS biodetection, and a thin magnetic film deposited on the side for magnetic actuation [Fig. 1(A-B)]. Diatoms are one of the most common and widespread types of photosynthetic microalgae, living abundantly in marine ecosystems. Frustules are the cell walls of diatoms made of silica with ordered arrays of nanopores [Fig. 1(C-D)]. These naturally existing and widely available biomaterials exhibit high mechanical strength and chemical stability, which suggest feasible applications as micro/nanomechanical devices.(*32*) The periodic nanopores coupled with the plasmonic Ag nanoparticles further support photonic-crystal-plasmonic resonance that substantially increases SERS for ultrasensitive molecule detection. (*33, 34*)

The detail of the fabrication of the above designed microsensor is discussed in the section of Materials and Methods. Briefly, to fabricate well-reproducible and high-quality micromotor-sensors, we disperse, sonicate, filter, and calcinate commercially-available diatomaceous earth powder to produce refined diatom frustules.(*32*) These processes remove both organic and inorganic impurities and broken pieces of frustules and deliver purified cylindrical diatom frustules with diameters of 8- 16 µm and lengths of 20 to 35 µm [Fig. 1(C)]. Next, A bilayer nickel (Ni)/gold (Au) thin film is deposited on one side of the diatom frustules with electron-beam evaporation for magnetic manipulation. In the end, high-density arrays of plasmonic Ag nanoparticles are synthesized uniformly on the surface of the diatom frustules for SERS detection [Fig. 1(E)].(*35, 36*) The average diameter is 23.38±3.30 nm and the junction ranges from 0.5 nm to 5 nm (Supporting Information Fig. S1).

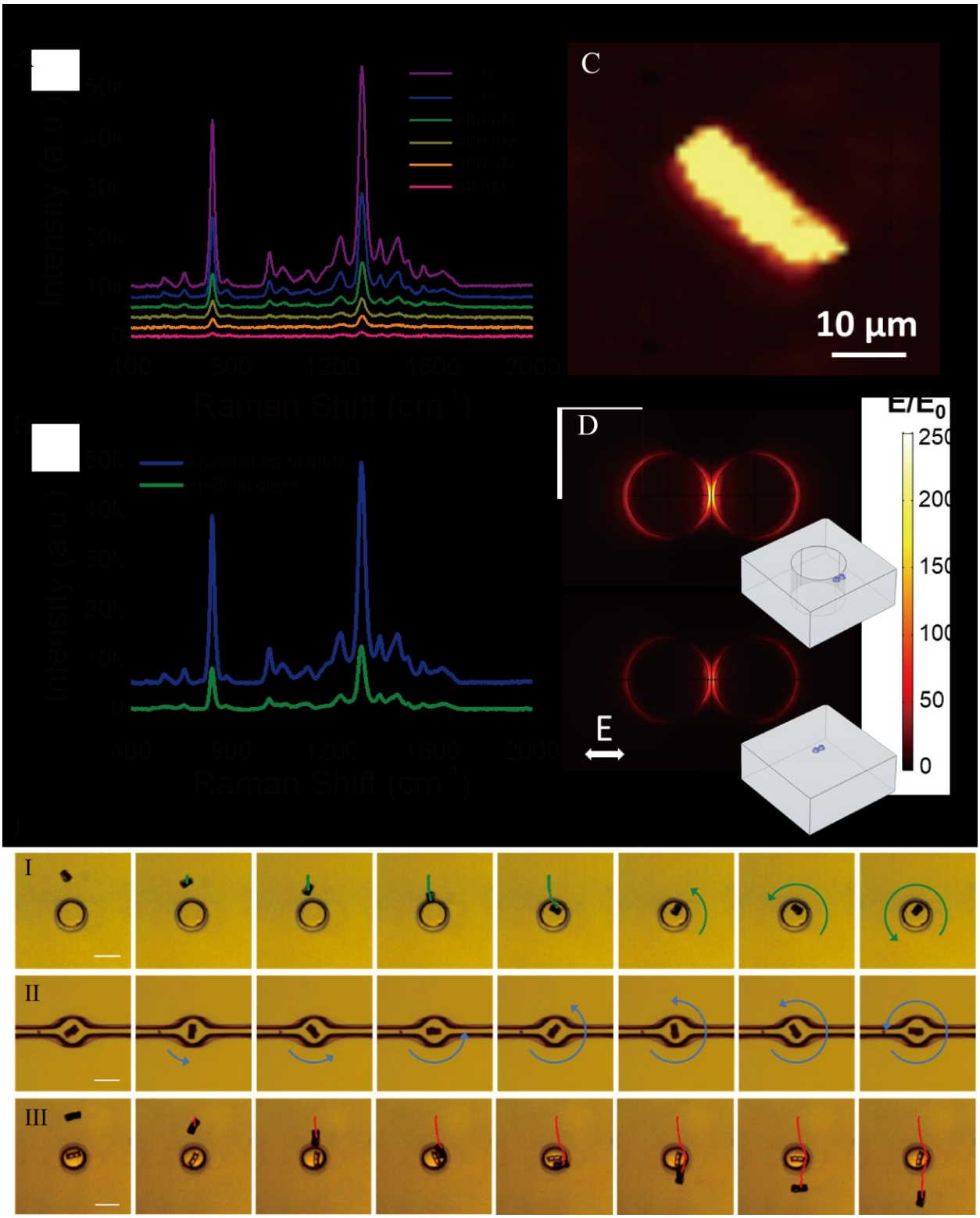

Figure 2. **Surface enhanced Raman spectroscopy of the micromotor-sensor and rotation-assisted assembly of micromotor-sensors in microfluidic wells.** (**A**) SERS spectra of DNA molecules of 80 nM to 4 µM. (**B**) Comparison of SERS spectra of DNA molecules (4 µM) on a microsensor (in blue) and on an Ag-nanoparticle coated flat glass substrate (in green). (**C**) Raman

mapping of DNA molecules (4 μM, 724 cm^{-1}) on a microsensor (2-hour incubation) shows signals with good uniformity. (**D**) Simulations of electric-field distribution around a pair of Ag nanoparticles placed on a diatom frustule (top) and flat glass (bottom). Insets: schematics of the respective structures with a pair of Ag nanoparticles. Incident laser is polarized horizontally. (**E**) I. A micromotor-sensor rotating and assembling into a microwell (Snapshots: every second in the first 5 seconds and then every 0.05 seconds). II. A micromotor-sensor stably rotates in a microfluidic channel (snapshots: every 0.025 seconds). III. A micromotor-sensor rotating at 300 rpm detoured around an occupied microwell (snapshots: every second, scale bar 30 μm).

Next, we studied the Raman sensitivity of the microsensors by testing Salmon sperm DNA molecules. Among various important biomolecules, DNA molecules are chosen due to their significant roles in medical diagnosis, treatment, and forensic investigation.(*37, 38*) As shown in Fig. 2(A), after incubation in DNA solutions of 80 nM to 4 μM for 2 hours, we can detect signals of DNA molecules with a concentration as low as ~80 nM with an averaged signal-to-noise ratio of 5 at 724 cm^{-1} and 1319 cm^{-1} (both from the vibration of nucleobase adenine).(*39*) The Raman intensity monotonically increases with the DNA concentration with a largely uniform enhancement along the length of the microsensors [Fig. 2(A)]. It was determined that the enhancement factor is up to ~ 10^9 to 10^{10} on the surface of Ag-nanoparticle-dispersed substrate fabricated with the same method and morphology.(*35, 40*) Moreover, compared to Ag nanoparticles grown on a flat glass substrate at the same condition, the Raman intensity shows additional improvement on the plasmonic diatom-frustule motor as high as 3.66 ± 0.31 times across all the major DNA peaks [Fig. 2(B)], *i.e.* 724 cm^{-1} (adenine), 957 cm^{-1} (deoxyribose moiety), 1235 cm^{-1} (thymine and cytosine), 1319 cm^{-1} (adenine) and 1391 cm^{-1} (guanine).(*39, 41*) The improvement in sensitivity can be attributed to the resonance of localized surface plasmon with the photonic-crystal nanopores on the surface of the diatom frustules.(*34*) As shown in the numerical simulation in Fig.2(D), at least 1.98 time increase in the electric-field intensity is found for a pair of Ag nanoparticles placed next to a nanopore compared to that on a flat glass substrate (Materials and Methods). This value can be higher as Ag nanoparticles distribute on a 3D surface. Furthermore, since the plasmonic Ag nanoparticles offer orders-of-magnitude Raman enhancement, while such enhancement only presents in the vicinity of the Ag nanoparticles and their narrow junctions, the so-called hotspots, we can safely consider that only the DNA molecules on the surface of the micromotor sensors are detected. The DNAs in the background suspension without the plasmonic enhancement essentially have no contribution to the collected Raman signals [Fig. 2(C)]. Therefore, we can readily monitor the dynamic capture process of the DNA molecules by the solid surface *in-situ* and in quasi-real-time owing to the near-field effect of SERS (SI note 1).

To detect biomolecules in a position-deterministic and robust manner for long-duration dynamic analysis, the as-obtained micromotor-sensors are integrated into individual microwells (or microchannels) via a self-assembly process assisted by magnetic rotation. Here, a tunable rotating magnetic field is applied from the top of the microsensors dispersed on the microfluidic device with arrays of microwells as shown in Fig. 1(A). A magnetic stirrer, commonly used in chemistry and biology labs, provides the magnetic field. The magnetic field is applied above the micromotor-sensors to allow the generation of magnetic force on a micromotor-sensor in the upward direction with the magnitude proportional to the magnetic-field-gradient, which balances the gravitational force and effectively reduces the hindering force from the substrate. This setup ensures stable and

durable rotational actuation of the micromotor-sensors. It is particularly useful for the capture and detection of various biomolecules in practice when the suspension is often complex and ionic that aggravates the interactions of a suspending microsensor with the wall.

It is found that with an applied magnetic field ($\boldsymbol{B}$), all dispersed micromotor-sensors rotate at a synchronous speed that can be tuned up to 1200 rpm (Supporting Information Fig. S2). The driving magnetic torque is given by $\boldsymbol{\tau_m} = \boldsymbol{m} \times \boldsymbol{B}$, where $\boldsymbol{m}$ is the magnetic moment of a micromotor-sensor. During the rotation, the microsensors slowly move on the Polydimethylsiloxane (PDMS) film and assemble into individual microwells (30 μm in diameter and 10 μm in height) [Fig. 2(E) and Movie S1]. Importantly, the assembly is accomplished in a one-on-one fashion: when one micromotor-sensor encounters a microwell that is already occupied by a rotating microsensor on its moving path, it detours around and moves forward (Movie S1). The one-on-one assembly can be robustly obtained owing to the fluidic repulsion between two close-by rotating motor sensors,(*42*) which is critical for long-time and reliable molecule capture and SERS detection.

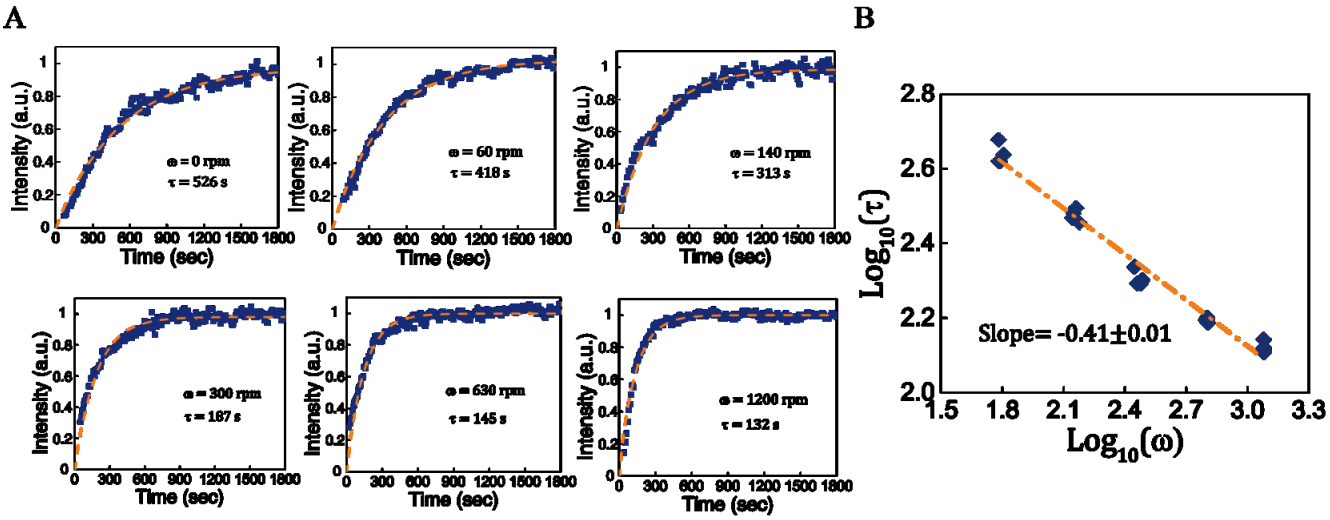

Figure 3. **Dynamics of the mechanical rotation accelerated capture process of DNA molecules revealed by SERS. (A)** Dynamics of the DNA capture process on a microsensor with various rotation speeds. (**B**) Log-log plot of the characteristic DNA capture time (in second) versus rotation speed (ω in rpm) of microsensors. The linear fitting from 60 rpm to 1200 rpm shows a slope of -0.41.

With all the above efforts on the design, fabrication, sensing characterization, and the one-on-one assembly of individual rotary sensor-in-well devices, we are able to study the impact of controlled mechanical rotation to the capture and detection efficiency of DNA molecules. Albeit remarkable efforts on the optimization of the binding buffers (*43-45*) and substrates (*46-48*), , the efficiency of the DNA capture remains poor, particularly for solutions of low molecular concentrations.(*49*) It can take tens of minutes to several hours to reach a capture saturation.(*50, 51*)
Now, we monotonically increase the rotation speed of the individually assembled micromotor-sensors up to 1200 rpm and detect the Raman signals from the body of the microsensor simultaneously. The DNA capture process is continuously monitored every 10 seconds for 30 minutes from a rotating sensor. The Raman intensity of DNA molecules always increases monotonically until it reaches a plateau on the microsensors as shown in Fig. 3(A). We found that

the mechanical rotation clearly accelerates the DNA capture and enrichment process. For instance, the required time to reach 95% of the capture equilibrium of DNA is reduced from ~ 28 minutes on a static microsensor, to ~ 7 minutes on a rotating microsensor at 1200 rpm, which is a 4-fold improvement [Fig. 3(A)]. Even at a speed of 300 rpm, the capturing process only requires 1/3 of the capture time of that with a static microsensor. We further obtain the characteristic time (τ) at different rotation speed (ω) by fitting the time-dependent Raman Intensity of DNA [Fig. 3(A)] with an exponential function given by $I = I_0\left[1 - \exp\left(-\frac{t}{\tau}\right)\right]$, and then plot the log-log dependent of τ versus ω [Fig. 3(B)]. It is found that the characteristic time τ monotonically decreases with the rotation speed ω from 60 rpm to 1200 rpm, with a power-law dependence of $\tau \sim \omega^{-0.41\pm0.01}$. The above series of experiments clearly evidence that the capture speed of DNA molecules can be remarkably enhanced with mechanical rotation as revealed by the dynamic capture process with Raman spectroscopy. To understand the mechanistic role of mechanical rotation in the enhancement of molecule capture, we carried out theoretical analysis and modeling. The results are implemented to provide a physics picture for this DNA molecule-motor-fluid system to be discussed as follows.

Theoretical Analysis and Modeling

Reaction-Diffusion-Convection Kinetics: The understanding of transport and reaction of diluted analyte molecules with their receptors is critical for the understanding of the working mechanism and limits of the modern micro/nanobiosensors. Great efforts have been spent on investigating the kinetics of such reaction-diffusion-convection systems from both the experimental and theoretical perspectives.(*11, 12, 52*) Three important interactive processes can be identified that govern the molecule capture kinetics by a solid surface, *i.e.*, the convection of analyte molecules driven by the flow, the diffusion of the analytes towards the solid surface, and the reaction on the solid surface [Fig. 4(A)]. When hard limits occur, it is usually one of the three processes becoming the rate-determining step. Thus, determining the rate-limiting process is essential for lowering the barrier towards a better performance.

When the fluidic flow is introduced into the system, the convection term of mass transport must be added into the transport equation in addition to the Fick's second law given by Equation (1):

$$\frac{\partial \mathrm{c}}{\partial \mathrm{t}} = \mathrm{D}\nabla^2 c - \mathbf{v} \cdot \nabla \mathrm{c}, \qquad (1)$$

where *c*, *D*, and *v* are the concentration of molecules, diffusion constant, and flow velocity, respectively. Convection is generally more effective in mass transport compared to that of the passive diffusion for most molecules.

To quantitatively solve the above complex convective-diffusion problem at low Reynolds numbers and to understand the behavior of our experimental system, our strategy is to divide the modeling into two sub-problems. First, we utilize numerical simulation to compute the convection-diffusion dynamics to study the diffusion boundary layer thickness as a function of the external flow rate. Here, we inherit the concept of Nernst Diffusion Layer with slight modification. Nernst assumed a layer with thickness δ_D in which only the diffusion occurs in a moving liquid. This layer is static and in the immediate vicinity of the solid surface. Beyond this layer, the molecule concentration is constant, the same as the bulk due to external convection. The clear physics picture provided by Nernst's theory, however, does not allow quantitative computation due to the unnatural definition of the boundary. In order to quantitatively determine

the boundary layer thickness with numerical simulation, we define the outer edge of the diffusion boundary layer wherever the concentration of the analyte equals to 90% of the bulk concentration. Then, we study a 1D reaction-diffusion kinetic problem within the static diffusion boundary layer, without the convection term. In our treatment, the convection plays the role in influencing the diffusion boundary layer thickness; within the diffusion boundary layer, the molecule transport dynamics is solely governed by the diffusion and reaction processes. We believe this strategy, differing from other works, can offer a clear physics pictures of the role that each factor plays in the system for the understanding of the underlying working mechanism of the experimentally observed mechanical motion enhanced detection of DNA molecules.

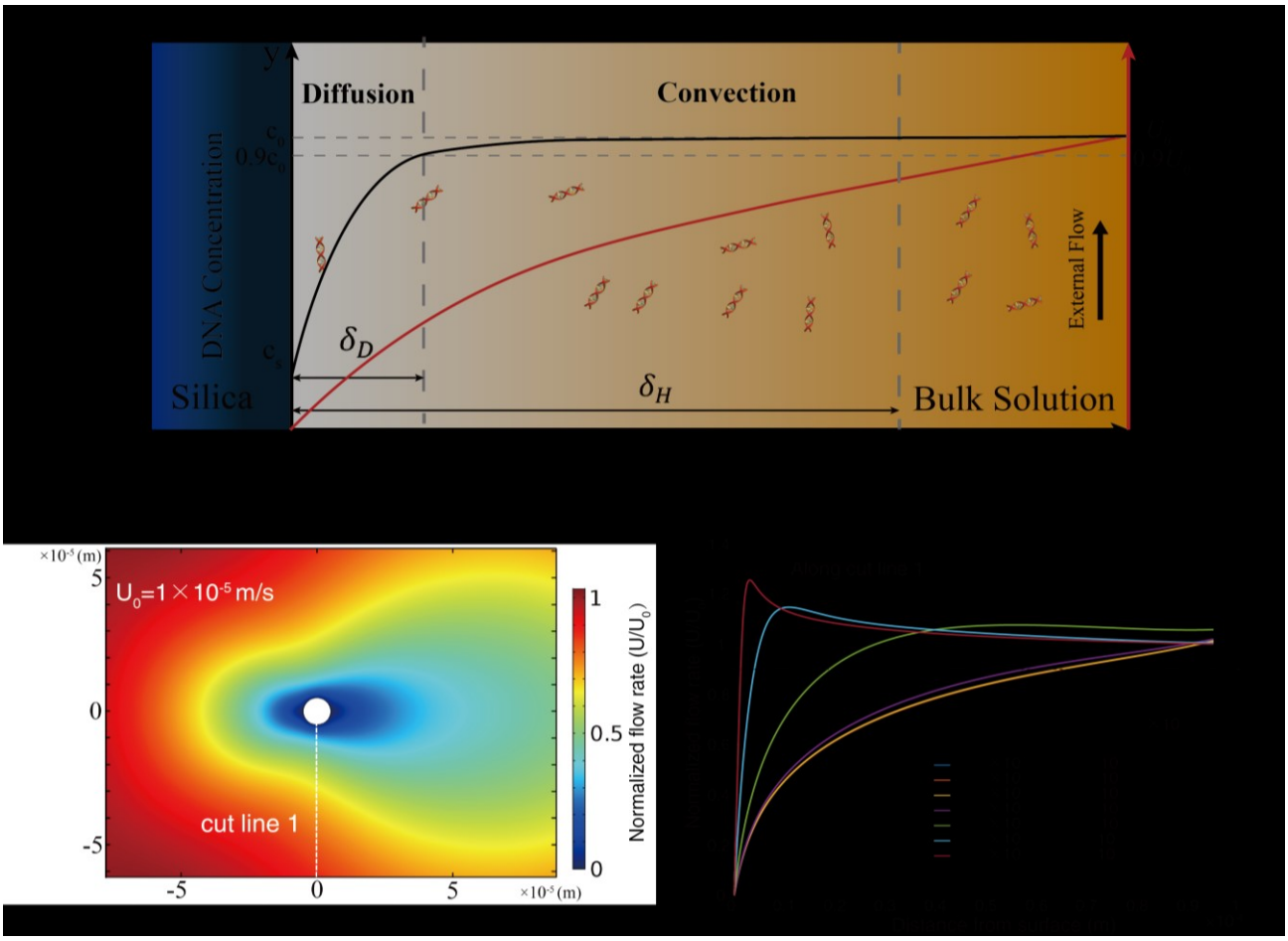

Figure 4. (A) Diagram of the DNA capture process involving reaction on a solid surface, diffusion and convection. (B) The profile of laminar flows passing across a circular cylinder (cross-section view) at a low Reynolds number of 1×10^{-4}. (C) Flow rate along the cut line 1 with various external flow rates (U_0).

Diffusion-Convection Kinetics: in the first step, we simplify the 3D model of a self-spinning microsensor to a 2D problem of laminar flow passing across a circular cylinder of 10 μm in diameter as shown in Fig. 4(B). The flow rate is varied from 10^{-5} m/s to 10 m/s, which corresponds to a Reynolds number from 10^{-4} to 100. The flow rate profile is mapped along the cut line 1 as shown in Fig. 4(C). On the surface, due to the none-slipping boundary condition, the flow rate is always zero. With the increase of the distance from the cylinder, the flow rate

monotonically increases to 90% of the external flow rate U_0, the location of which is defined as the outer edge of the hydrodynamic boundary layer with a thickness of δ_H. For systems with a Reynolds number Re $>10^{-2}$, the dimensionless flow profile changes significantly, the increase of the external flow rate U_0 results in the decrease of δ_H, and at high Reynolds numbers, the dependence of δ_H on U_0 approximates to $\delta_H \sim U_0^{-0.5}$ as predicted by the Prandtl's boundary layer theory.(*53*) On the other side, at a low Reynolds number, *i.e.*, a system with Re $\leq 10^{-3}$, the normalized flow profiles remain largely the same, indicating that the hydrodynamic boundary layer thickness δ_H is independent of the external flow rate at an extremely low Reynolds number, which is a characteristic of Stokes flow.

Although the flow profiles after normalization by the external flow rate U_0 are almost identical for various flow rates when $U_0 < 1 \times 10^{-3}$ m/s, the convection term in Eq. (1), which is directly proportional to the flow rate, can be enhanced. Here, we further simulate the convective diffusion of DNA, carried by external flow rate ranging from 1.00×10^{-5} m/s to 2.51×10^{-3} m/s passing around the same cylinder with a fast reaction boundary condition $c = 0$ at the cylinder surface, and assume that the incoming flow carries the same concentration c_0. The concentration profile is probed when the system is fully developed [Fig. 5(A-C)]. In particularly, we monitor the concentration profile along the cut lines 1, 2 [Fig. 5(A)] under different external flow rates as shown in Fig. 5(D-E). The concentration profile is significantly altered by the flow. With the increase of the external flow rate U_0, the concentration gradient increases, and the thickness of the diffusion boundary layer (δ_D) decreases accordingly. This result indicates that even in a low Reynolds number region, the enhancement of convection in mass transport by flow is still effective and practically useful. We summarize the result of both the hydrodynamic boundary layer thickness (δ_H) and diffusion boundary layer thickness (δ_D) as a function of the external flow rate in Fig. 5(F). The fitting of diffusion boundary layer δ_D as a function of the external flow rate U_0 determines a dependence of $\delta_D \sim U_0^{-0.349 \pm 0.015}$ at the front side, and $\delta_D \sim U_0^{-0.341 \pm 0.022}$ on the top and bottom of the cylinder. The slight difference among different locations on the cylinder allows us to adopt an average value to represent the dependence as $\delta_D \sim U_0^{-0.344 \pm 0.020}$ for the further analysis.

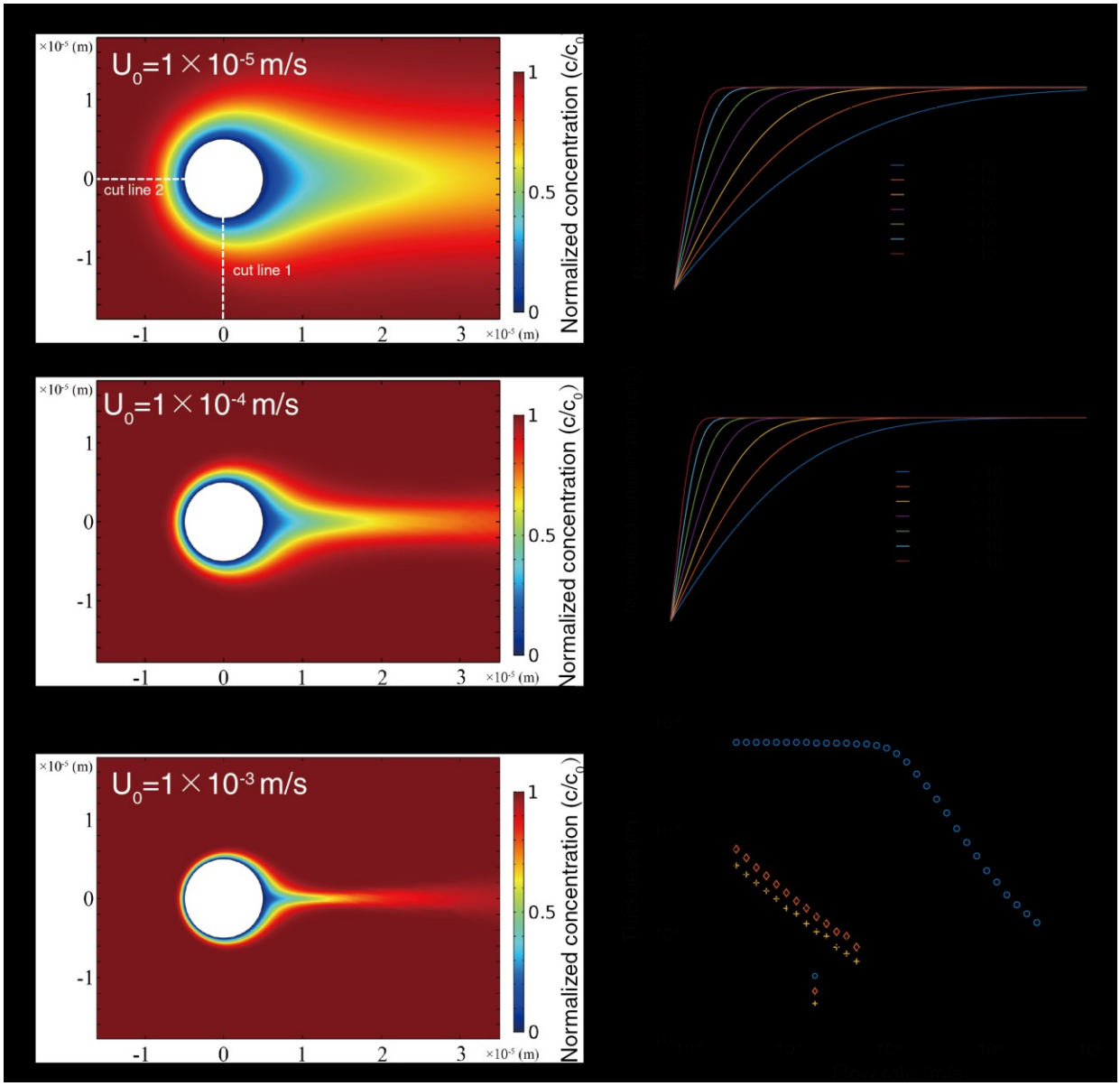

Figure 5. Simulation result of the convective diffusion at low Reynolds numbers. (A-C) the concentration profile of laminar external flow with various flow rates U_0 carrying DNA molecules passing around a reactive cylinder surface with zero concentration. (D) The normalized concentration along cut line 1 under different external flows and (E) along cut line 2. (F) The thickness of hydrodynamic (in blue) layer and diffusion boundary layer (in red) versus flow rate.

Reaction-Diffusion Kinetics: in the above, we model the convection-diffusion dynamics with a simplified fast reaction boundary condition to extract the impact of external flows to the thickness of the hydrodynamic and diffusion layers. The obtained power dependence on flow rate is valid not only for fast reaction conditions but also for the conditions when the surface reaction does not consume all transported molecules. Next, we start the investigation of a 1-D molecule reaction-diffusion system without convection (the effect of convection has been considered by the dependence of δ_D on U_0). The system consists of a reactive solid surface, *i.e.,*

the silica surface of the micromotor sensor, which captures DNA molecules via adsorption, as well as a diffusion boundary layer with thickness of δ_D, across which the concentration of DNA can vary with time (t) and position (x). We use the following Fick's second law:

$$\frac{\partial c}{\partial t} = D\nabla^2 c \qquad (2)$$

where c and D are the volumetric concentration and diffusivity of the DNA molecules, respectively. To solve this equation, two boundary conditions are required at the edges of the domain of interest. The first boundary condition at the outer edge of the diffusion boundary layer is given by: $c = c_0$, at $x = \delta_D$. The second boundary condition involves the surface reaction at the silica/solution interface. Given the mass conservation, the flux of the analytes going towards the surface has to be equal to the instantaneous adsorption rate of analytes at the surface, which can be written as: $\frac{\partial n}{\partial t} - D\frac{\partial c}{\partial x} = 0$, *at* $x = 0$. Here we assume that Fick's first law is valid at low concentration and define a surface adsorption density as n, which is the number of absorbed DNA molecules per unit area by the silica surface. Here, the surface adsorption kinetic can be described by the Langmuir isotherm as follows:

$$\frac{\partial n}{\partial t} = k_a(n_{max} - n)c_s - k_d n, \qquad (3)$$

where k_a, n_{max}, c_s , and k_d are the adsorption coefficient, maximum surface adsorption density, surface concentration of analyte molecules in the solution immediately next to the solid surface, and desorption coefficient, respectively (SI note 2, Fig. S3).

To get insights of the reaction-diffusion kinetics, we further non-dimensionalize the equations (2-3) (SI note 3), and numerically solve the 1D reaction-diffusion problem with the finite differential time domain (FDTD) method (Details in SI note 4). The results determine that the molecule transport kinetics depends on the Damköhler number of the system, which is defined by the ratio of the reaction and diffusion rates given by $Da = \frac{\delta_D n_{max} k_a}{D}$ (SI note 3). When the system reaches an equilibrium, the surface concentration c_s becomes c_0, and the surface density is given by $n_{eq} = \frac{k_a n_{max} c_0}{k_a c_0 + k_d}$. Let $\tilde{c} = \frac{k_a c_0}{k_d}$, n_{eq} can then be written as $n_{eq} = \frac{\tilde{c}}{1+\tilde{c}} n_{max}$. In the simulation, the range of the Damköhler number is selected from $0.001\ to\ 1000$ that covers the surface-adsorption-reaction limited process when it is ultrasmall, *i.e.*, $Da \ll 1$, and the diffusion limited process when it is large, *i.e.*, $Da \gg 1$.

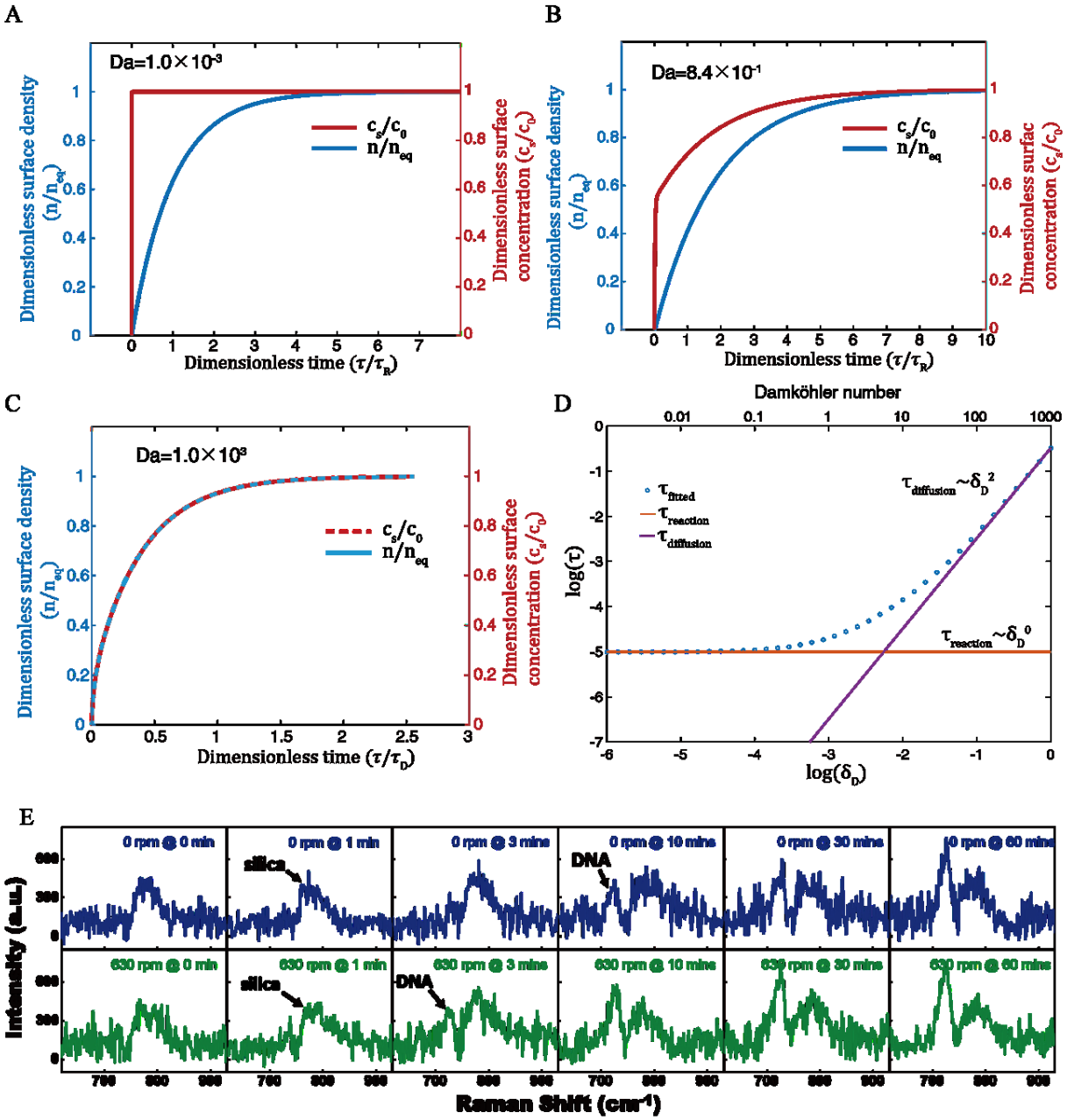

Figure 6. Simulation of the reaction-diffusion kinetics at different Damköhler numbers and demonstration of rotation accelerated detection of low-concentration DNA molecules. (A-C) The evolution of surface adsorption density and surface concentration with (A) Da=1000, (B) Da=0.84, and (C) Da=0.001. (D) The characteristic time scales of the reaction-diffusion process obtained by fitting at different thicknesses of diffusion layers. (E) Raman spectra of low-concentration DNA molecules (80nM) measured at fixed time intervals for an hour on (a) a static (in blue) and (b) on a rotating microsensor with speed of 630 rpm (in green).

Three sets of representative systems with Da numbers of 10^{-3}, 8.4×10^{-1} and 10^{3} are evaluated to show the evolution of both the molecular surface adsorption density (n) (in blue) and concentration of molecules next to the surface (c_s) (in red). At Da=10^{-3}, where the system is in the reaction-rate limited regime, the diffusion process quickly reaches equilibrium as shown by

the steep step-like function in red in [Fig. 6(A)]. Due to the low reaction speed, the surface density of molecules versus time (n) follows an exponential function given by $n(t) = n_{eq}[1 - \exp\left(-\frac{t}{\tau_R}\right)]$, where $\tau_R = \frac{1}{k_d(1+\tilde{c})}$ (SI note 2). At Da=10^3, the time-dependent dimensionless n/n_{eq} and c/c_s essentially overlap [Fig. 6(C)]. This is a result of the diffusion limited process, where the reaction goes through a quasi-static process controlled by the speed of the diffusion. Here, the molecular concentration gradient is the driving force of the diffusion flux that n/n_{eq} is always close to but slightly lower than c/c_s in the same time scale. Finally, for a system with an intermediate Da number of 0.84, the reaction and diffusion rates are comparative, and the kinetics is governed by both diffusion and reaction [Fig. 6(B)].

We further calculate the characteristic time of molecule transport (τ) at different Da numbers for a system, where δ_D is the only varying parameter that can be changed by an external flow speed. The value of τ is obtained via fitting the time-dependent molecular surface density (n) with $\frac{n}{n_{eq}} = 1 - \exp\left(-\frac{t}{\tau}\right)$ as shown in [Fig. 6(D)]. When the diffusion layer is thin that corresponds to a small Da number and a reaction limited process, the value of τ is essentially a constant (red tangent line in [Fig. 6(D)]). This agrees with our earlier discussion that the reaction time constant is given by $\tau_R = \frac{1}{k_d(1+\tilde{c})} \sim \delta_D^0$, independent of δ_D. With the increase of δ_D, the process becomes diffusion dominated and τ scales with ${\delta_D}^2$ as given by the time constant of diffusion $\tau_D = \frac{\delta_D^2}{D}$, shown by the purple tangent line and data points at the high Da-number region. In between the two extremes, $\tau \sim \delta_D^p$, and the power coefficient p ranges from 0 to 2. From the above, it can be found that the molecular transport dynamics in a diffusion-reaction system highly depends on the thickness of the diffusion layer that can be modulated by external flows.

Understanding of the experimental results with the modeling

The above modeling can be readily applied to provide insights to our experimental results. As shown in Fig. 3, we observed remarkable acceleration of DNA capture by the rotating microsensors. The fitting shows that the characteristic time (τ) follows a power-law dependence of $\tau \sim \omega^{-0.41\pm0.01}$ on the rotation speed ω. Since the highest rotation speed tested in the experiment is 1200 rpm, corresponding to a Reynolds number of approximately 0.01, all the experimental conditions are within the low Reynolds number region. Therefore, for our system it is feasible to use the dependence of $\delta_D \sim U_0^{-0.34\pm0.03}$ as shown in Fig. 5(F). Also, because the external flow rate U_0 is proportional to the rotation speed ω, we can readily obtain $\delta_D \sim U_0^{-0.34} \sim \omega^{-0.34}$. Now, combining the dependence of $\delta_D \sim \omega^{-0.34}$ from the numerical simulation and $\tau \sim \omega^{-0.41}$ from the experiments, we can readily determine the relation of $\tau \sim \delta_D^{1.21}$, which corresponds to a Damköhler number of 20. This Da number indicates that the overall rate-limiting step is the diffusion process in this DNA capture system. This result obtained by the analysis with the modeling also agrees with the temperature-dependent experimental results of the DNA adsorption [Fig. S4].

It is known that the adsorption of DNA molecules on the silica surface is a process consisting of both kinetic association and disassociation, and the kinetic association in a binding buffer with a pH value lower than 7 is an exothermic process.(*54*) Therefore, the adsorption rate of DNA is expected to decrease with temperature. Oppositely, the diffusion process is facilitated by higher temperature. Clearly, these two temperature-dependent effects are countering to each other. As

shown in Fig. S4, we found that the adsorption rate of DNA monotonically increases with temperature, which agrees with the situation suggested by the modeling that it is the diffusion of DNA molecules limiting the overall capture kinetics. Therefore, the role of mechanical rotation can be understood. The rotation and the resulted flow convection effectively reduce the diffusion layer thickness (δ_D), and in turn increase the DNA diffusion rate, which is the kinetic limiting step of the overall reaction. The rotation, as a result, can be utilized to substantially increase the capture efficiency of DNA molecules. The higher the rotation speed, the narrower the diffusion layer, and the greater the capture efficiency. Since the value of the demonstrated Damköhler number of around 20, still has room to improve, we expect the DNA capture speed can be even more enhanced with higher rotation speed.

Finally, with the above understanding, we further demonstrate the first successful enhancement of detection efficiency of low-concentration DNA molecules by mechanically rotating a micro/nanosensor. Samples with a DNA concentration of 80 nM are tested on both static and rotating microsensors as shown in [Fig. 6(E)]. The speed of rotation is 630 rpm. Fig. 6 presents the obtained time-dependent Raman spectra of DNA molecules. The Raman peak at ~780 cm^{-1} from silica remains constant during the detection showing the invariance of the sensitivity of the microsensors under the mechanical rotation. The Silica peak is used as a reference for comparison with DNA signals. On the static microsensor, the Raman signal of DNA at 724 cm^{-1} can be hardly observed in the first 3 minutes and becomes gradually clear at ~ 10 minutes. From the rotating microsensor, however, it takes only 3 minutes to exhibit the Raman signal of DNA molecules with an intensity similar to that obtained at around 10 minutes from the static microsensor. The improvement is ~ 3 folds in detection speed, confirming the feasibility in obtaining enhanced detection speed of low-concentration molecules with motorized micro/nanosensors. The result has been robustly observed in multiple repeats.

Discussion and Summary

In summary, we report an innovative and effective strategy to realize mechanical rotation enhanced capture and detection of low-concentration biomolecules. The opto-plasmonic microsensors made of diatom frustules provide silica surface chemistry for DNA capture, and periodic nanopore arrays coupled with dense plasmonic Ag hotspots for sensitive and quasi-real-time dynamic SERS sensing. The microsensors are transported and self-assembled in individual microfluidic wells or channels that enables the desired position-deterministic sensing of DNA molecules during high-speed rotation. The mechanical rotation effectively accelerates the capture process for DNA molecules, i.e., 4 times at a speed of 1200 rpm. This strategy is particularly advantageous in its low requirement of sample volume, which can rapidly accumulate interesting molecules by self-spinning induced localized flow. In comparison, for microfluidic-based passive biosensors, if enhancing by analyte flows, a large volume of samples generally should be prepared. Moreover, in this work, we understand the fundamental working mechanism of motorization enhanced sensing by analysis, modeling and simulation. We find that to enhance the performance of such micro/nanoscale biosensors, it is critical to estimate the dimensionless Damköhler number, which represents the ratio between the reaction and transport rates of molecules. For a high-Da-number system, e.g. passive diffusion of macromolecules, strategies should be devoted to the enhancement of mass transportation. The mechanical motorization is a feasible and effective approach. For a low-Da-number system, e.g. small molecules with convective diffusion, the reaction kinetics

should be improved for higher efficiency. The modeling approach could also be useful in understanding the molecule-nanoobject interactions often observed in micro/nanorobotics operating in aqueous environments. It could be used to guide the design and optimization of micro/nanomotors, machines, and robots for molecular capture, sensing, and delivery, in which low Reynolds number hydrodynamics and reaction-diffusion kinetics play immense roles. Overall, the device design, characterization, application, as well as modeling and simulation presented in this work could inspire innovative device schemes for high-speed biochemical enrichment, sensing, reaction, and release that are relevant to biodetection, delivery, and micro/nanorobotics.

Materials and Methods

Fabrication of Bio-Opto-Plasmonic Microsensors:

Preparation of diatom frustules: the diatomaceous earth powders are purchased from Natural Gardener (Austin, TX) at a price of 1 dollar per pound. The diatom frustules used in this work are processed and refined via dispersion, sonication (2 minutes), and filtration in D.I. water. Impurities and broken pieces of frustules are filtered out by filter papers (VWR® Grade 417 Filter Paper, size of particle retention: 40 μm). The diatom frustules are then calcinated in air at 500 ˚C for 2 hours to remove organic residues.

Deposition of magnetic thin film: the magnetic thin film on diatom frustules consists of 20 nm Ni and 20 nm Au, which are deposited by electron-beam evaporation. Here the Au layer works as a passivation layer that prevents magnetic aggregation of the diatom frustules in suspension.

Synthesis of plasmonic Ag nanoparticles: Ag nanoparticles are synthesized on the surfaces of diatom frustules by catalytic reduction of silver nitrate ($AgNO_3$). Firstly, the diatom frustules are incubated and stirred in the mixture of $AgNO_3$ (0.06 M, 500 μL) and ammonia (0.12 M, 250 μL) for sufficient adsorption of Ag ions. Then polyvinylpyrrolidone (PVP, 10 mL of 2.5×10-5 M in ethanol) is added to promote the reduction of $AgNO_3$ and growth of Ag nanoparticles at 70 ˚C. After 7-hour reaction, dense Ag nanoparticles are uniformly synthesized on the surface of diatom frustules. Finally, after rinsing in ethanol and D.I. water (repeated processes of centrifugation and dispersion), the microsensors based on diatom frustules are stored in D.I. water.

Numerical Simulation of Electromagnetic Fields on Plasmonic Nanoparticle Dimers by COMSOL: The Ag nanoparticles are modeled as hemispheres of 25 nm in diameter with junctions of 2 nm. The porous microstructure of diatom frustule is modeled as a photonic silica substrate with 2-dimentional periodic nanopores of 300 nm in diameter with position periodicity of 1.2 μm in both X and Y directions. The Ag nanoparticle dimer is placed on the edge of the nanopore. For comparison, a pair of same Ag nanoparticle dimer is placed on flat silica substrate. Both are excited with an in-plane polarized 532-nm laser.

Capture and Detection of DNA Molecules on Microsensors:

Materials: salmon sperm DNA used for the demonstration is purchased from Invitrogen @ Thermo Fisher Scientific (Carlsbad, CA). As stated by the manufacturer, the DNA is extracted by phenol-chloroform and sheared to an average size of < 2000 bp. The composition of binding buffer is 50 mM tris(hydroxymethyl)aminomethane (Tris), 0.25 mM acetic acid, and 400 mM potassium ions(K+), with pH adjusted to 4. Potassium hydroxide (KOH) or hydrochloric acid (HCl) is used to adjust the pH value.

DNA capture: the DNA solutions (2× predetermined concentrations) are pipetted and rapidly mixed with the binding buffers (3× predetermined concentrations) and the suspensions of microsensors with a volume ratio of 3:2:1. For the capture dynamics characterized by Surface-Enhanced Raman Spectroscopy (SERS), the DNA concentration in the mixture is 500 μg/mL, the total volume of solution after mixing is 18 μL, and the weight percentage of microsensors in suspension is ~ 10 μg/mL. At this concentration, there are only a few microsensors in the mixed

solution. In this case, the DNA concentration in the bulk solution can be considered a constant during the capture process because very low amount of DNA is captured.

For the capture dynamics characterized by Ultraviolet (UV) absorbance spectroscopy, the DNA concentration in the mixture is 500 μg/mL, the total volume of solution after mixing is 120 μL, and the weight percentage of microsensors in suspension is ~ 50 mg/mL. In this case, large amount of DNA molecules is captured so that the concentration change of DNA in the solution is detectable by the UV spectroscopy. The DNA capture dynamics at different temperatures are conducted in refrigerator (at 5 ˚C) or in thermostatic water bath (at 25 ˚C and 45 ˚C, respectively). The DNA solutions, binding buffers and the suspensions of microsensors are all pre-cooled or pre-heated at a designated temperature for 30 minutes before mixing.

SERS characterization: the microsensors are incubated in DNA solutions with concentrations ranging from 80 nM to 4 μM for 2 hours before measurements. A 532-nm laser with a spot of ~25 μm and power of 500 μW is used for SERS measurements. The exposure time for each test is 2 seconds. In Raman mapping, a 532-nm laser with a spot size of 1 μm and power of 100 μW is used. The exposure time for each testing point is 1 second.

Capture dynamics characterized by SERS: once the DNA solutions and binding buffers are pipetted and rapidly mixed with the suspension of microsensors, the concentrations of DNA molecules captured on the static or rotating microsensors are detected continuously. The laser has a spot size of ~ 25 μm so that the DNA molecules captured on the entire microsensors can be detected. The laser power is 500 μW. The exposure time for each testing point is 10 seconds.

Capture dynamics characterized by UV spectroscopy: since the DNA capture dynamics at different temperatures are conducted in refrigerator or in thermostatic water bath, the process cannot be monitored by SERS in quasi-real-time. A DNA solution sample (1 μL) is taken at a premeditated time for every UV spectroscopy measurement. The DNA concentrations are determined by using NANODROP 1000 spectrophotometer (Thermo Fisher Scientific) and the final results are averages of 5 tests.

References and Notes

1. S. M. Nie, S. R. Emery, Probing single molecules and single nanoparticles by surface-enhanced Raman scattering. *Science* **275**, 1102-1106 (1997).
2. A. M. Armani, R. P. Kulkarni, S. E. Fraser, R. C. Flagan, K. J. Vahala, Label-free, single-molecule detection with optical microcavities. *Science* **317**, 783-787 (2007).
3. F. Vollmer, S. Arnold, Whispering-gallery-mode biosensing: label-free detection down to single molecules. *Nature Methods* **5**, 591-596 (2008).
4. S. S. Acimovic, M. P. Kreuzer, M. U. Gonzalez, R. Quidant, Plasmon Near-Field Coupling in Metal Dimers as a Step toward Single-Molecule Sensing. *Acs Nano* **3**, 1231-1237 (2009).
5. A. Kinkhabwala *et al.*, Large single-molecule fluorescence enhancements produced by a bowtie nanoantenna. *Nature Photonics* **3**, 654-657 (2009).
6. Y. Weizmann, F. Patolsky, I. Willner, Amplified detection of DNA and analysis of single-base mismatches by the catalyzed deposition of gold on Au-nanoparticles. *Analyst* **126**, 1502-1504 (2001).
7. E. D. Goluch *et al.*, A bio-barcode assay for on-chip attomolar-sensitivity protein detection. *Lab on a Chip* **6**, 1293-1299 (2006).
8. X. Yao *et al.*, Sub-attomole oligonucleotide and p53 cDNA determinations via a high-resolution surface plasmon resonance combined with oligonucleotide-capped gold nanoparticle signal amplification. *Analytical Biochemistry* **354**, 220-228 (2006).
9. P. S. Waggoner, M. Varshney, H. G. Craighead, Detection of prostate specific antigen with nanomechanical resonators. *Lab on a Chip* **9**, 3095-3099 (2009).
10. G. F. Zheng, X. P. A. Gao, C. M. Lieber, Frequency Domain Detection of Biomolecules Using Silicon Nanowire Biosensors. *Nano Letters* **10**, 3179-3183 (2010).
11. P. E. Sheehan, L. J. Whitman, Detection limits for nanoscale biosensors. *Nano Letters* **5**, 803-807 (2005).
12. T. M. Squires, R. J. Messinger, S. R. Manalis, Making it stick: convection, reaction and diffusion in surface-based biosensors. *Nature Biotechnology* **26**, 417-426 (2008).
13. W. Wang, T.-Y. Chiang, D. Velegol, T. E. Mallouk, Understanding the efficiency of autonomous nano-and microscale motors. *Journal of the American Chemical Society* **135**, 10557-10565 (2013).
14. D. Singh *et al.*, Interface-mediated spontaneous symmetry breaking and mutual communication between drops containing chemically active particles. *Nature Communications* **11**, 1-8 (2020).
15. K. Kim, J. Guo, Z. Liang, D. Fan, Artificial micro/nanomachines for bioapplications: Biochemical delivery and diagnostic sensing. *Advanced Functional Materials* **28**, 1705867 (2018).
16. S. Palagi, P. Fischer, Bioinspired microrobots. *Nat Rev Mater* **3**, 113 (2018).
17. J. Li, B. E.-F. de Ávila, W. Gao, L. Zhang, J. Wang, Micro/nanorobots for biomedicine: Delivery, surgery, sensing, and detoxification. *Science Robotics* **2**, (2017).
18. L. Zhang *et al.*, Artificial bacterial flagella: Fabrication and magnetic control. *Applied Physics Letters* **94**, 064107 (2009).
19. S. Ghosh, A. Ghosh, Mobile nanotweezers for active colloidal manipulation. *Science Robotics* **3**, eaaq0076 (2018).

20. X. Ma, A. C. Hortelão, T. Patiño, S. Sánchez, Enzyme catalysis to power micro/nanomachines. *ACS nano* **10**, 9111-9122 (2016).
21. K. Melde, A. G. Mark, T. Qiu, P. Fischer, Holograms for acoustics. *Nature* **537**, 518-522 (2016).
22. Z. Wu *et al.*, A swarm of slippery micropropellers penetrates the vitreous body of the eye. *Science advances* **4**, eaat4388 (2018).
23. Z. Liang, D. Teal, D. Fan, Light programmable micro/nanomotors with optically tunable in-phase electric polarization. *Nature communications* **10**, 1-10 (2019).
24. L. Ren *et al.*, 3D steerable, acoustically powered microswimmers for single-particle manipulation. *Science advances* **5**, eaax3084 (2019).
25. H. Xie *et al.*, Reconfigurable magnetic microrobot swarm: Multimode transformation, locomotion, and manipulation. *Sci. Robot* **4**, (2019).
26. A. Aghakhani, O. Yasa, P. Wrede, M. Sitti, Acoustically powered surface-slipping mobile microrobots. *Proceedings of the National Academy of Sciences* **117**, 3469-3477 (2020).
27. J. Yu *et al.*, Active generation and magnetic actuation of microrobotic swarms in bio-fluids. *Nature Communications* **10**, 1-12 (2019).
28. S. Schuerle *et al.*, Synthetic and living micropropellers for convection-enhanced nanoparticle transport. *Sci. Adv.* **5**, eaav4803 (2019).
29. Y. Zhang *et al.*, Real-time tracking of fluorescent magnetic spore–based microrobots for remote detection of C. diff toxins. *Sci. Adv.* **5**, eaau9650 (2019).
30. J. Wu *et al.*, Motion-based DNA Detection Using Catalytic Nanomotors. *Nature Communications* **1**, 36 (2010).
31. B. Esteban-Fernández de Ávila *et al.*, Single Cell Real-Time miRNAs Sensing Based on Nanomotors. *ACS Nano* **9**, 6756-6764 (2015).
32. K. Kim, Z. X. Lang, M. L. Liu, D. L. Fan, Biobased High-Performance Rotary Micromotors for Individually Reconfigurable Micromachine Arrays and Microfluidic Applications. *Acs Appl Mater Inter* **9**, 6144-6152 (2017).
33. J. Clayton *et al.*, Electroluminescence and Photoluminescence from Nanostructured Diatom Frustules Containing Metabolically Inserted Germanium. *Adv. Mater.* **20**, 2633-2637 (2008).
34. F. Ren, J. Campbell, X. Wang, G. L. Rorrer, A. X. Wang, Enhancing surface plasmon resonances of metallic nanoparticles by diatom biosilica. *Optics express* **21**, 15308-15313 (2013).
35. X. B. Xu, K. Kim, H. F. Li, D. L. Fan, Ordered Arrays of Raman Nanosensors for Ultrasensitive and Location Predictable Biochemical Detection. *Advanced Materials* **24**, 5457-5463 (2012).
36. X. B. Xu, K. Kim, D. L. Fan, Tunable Release of Multiplex Biochemicals by Plasmonically Active Rotary Nanomotors. *Angew. Chem. Int. Ed.* **54**, 2525-2529 (2015).
37. M. A. Kutzler, D. B. Weiner, DNA vaccines: ready for prime time? *Nat. Rev. Genet.* **9**, 776-788 (2008).
38. M. A. Jobling, P. Gill, Encoded evidence: DNA in forensic analysis. *Nat. Rev. Genet.* **5**, 739-751 (2004).
39. G. J. Lee, Y.-W. Kwon, Y. H. Kim, E. H. Choi, Raman spectroscopic study of plasma-treated salmon DNA. *Appl. Phys. Lett.* **102**, 021911 (2013).

40. J. Liu, J. Guo, G. Meng, D. Fan, Superstructural Raman Nanosensors with Integrated Dual Functions for Ultrasensitive Detection and Tunable Release of Molecules. *Chem. Mater.* **30**, 5256-5263 (2018).
41. L.-J. Xu *et al.*, Label-Free Surface-Enhanced Raman Spectroscopy Detection of DNA with Single-Base Sensitivity. *J. Am. Chem. Soc.* **137**, 5149-5154 (2015).
42. B. A. Grzybowski, H. A. Stone, G. M. Whitesides, Dynamic self-assembly of magnetized, millimetre-sized objects rotating at a liquid–air interface. *Nature* **405**, 1033-1036 (2000).
43. R. M. M. Smeets *et al.*, Salt Dependence of Ion Transport and DNA Translocation through Solid-State Nanopores. *Nano Lett.* **6**, 89-95 (2006).
44. P. E. Vandeventer *et al.*, Multiphasic DNA Adsorption to Silica Surfaces under Varying Buffer, pH, and Ionic Strength Conditions. *J. Phys. Chem. B* **116**, 5661-5670 (2012).
45. F. J. Huang, H. J. Liang, Adsorption Behaviors of DNA/Cation Complexes on Amino and Silica Chip Surfaces: A Dual Polarization Interferometry Study. *ACS Appl. Mater. Interfaces* **5**, 5025-5033 (2013).
46. L. Ulrike, V. Caroline, P. V. K., G. M. A. M., Droplet‐Based DNA Purification in a Magnetic Lab on a Chip. *Angew. Chem. Int. Ed.* **45**, 3062-3067 (2006).
47. Y. Zhang *et al.*, A Simple Thermoplastic Substrate Containing Hierarchical Silica Lamellae for High-Molecular-Weight DNA Extraction. *Adv. Mater.* **28**, 10630-10636 (2016).
48. P. A. Johnson, M. A. Gaspar, R. Levicky, Polymer-anchored DNA gene monolayers. *Journal of the American Chemical Society* **126**, 9910-9911 (2004).
49. C. Katevatis, A. Fan, C. M. Klapperich, Low concentration DNA extraction and recovery using a silica solid phase. *PLOS ONE* **12**, e0176848 (2017).
50. X. Li, J. Zhang, H. Gu, Adsorption and Desorption Behaviors of DNA with Magnetic Mesoporous Silica Nanoparticles. *Langmuir* **27**, 6099-6106 (2011).
51. P. E. Vandeventer, J. Mejia, A. Nadim, M. S. Johal, A. Niemz, DNA Adsorption to and Elution from Silica Surfaces: Influence of Amino Acid Buffers. *J. Phys. Chem. B* **117**, 10742-10749 (2013).
52. R. Hansen, H. Bruus, T. H. Callisen, O. Hassager, Transient convection, diffusion, and adsorption in surface-based biosensors. *Langmuir* **28**, 7557-7563 (2012).
53. W. M. Deen, Analysis of transport phenomena. (1998).
54. K. A. Melzak, C. S. Sherwood, R. F. B. Turner, C. A. Haynes, Driving forces for DNA adsorption to silica in perchlorate solutions. *J. Colloid Interface Sci.* **181**, 635-644 (1996).

Acknowledgments

Funding: We thank the support of the National Science Foundation (Grants 1710922 and1930649) and Welch Foundation (Grant F-1734). J.G. thanks the International Student Research Fellowship from the Howard Hughes Medical Institute (HHMI).
Author contributions: J.G. carried out the experimental design, and data collection. Z.L. conducted the modeling, simulation, and analysis. D.F. conceived and supervised this project. K.K. contributed to the preparation of diatom frustules. P.V. selected the DNA molecules and suspension medium. All authors wrote and reviewed the manuscript.
Competing interests: The authors declare that they have no competing interests.
Data and materials availability: All data for the conclusion in the paper are present in the paper and/or Supplementary Materials. Contact D.F. for additional information.